

1 **Non-Equilibrium Fractionation Factors for D/H and $^{18}\text{O}/^{16}\text{O}$ During Oceanic**
2 **Evaporation in the North-West Atlantic Region**

3 D. Zannoni¹, H. C. Steen-Larsen¹, A. J. Peters², S. Wahl¹, H. Sodemann¹ and A. E.
4 Sveinbjörnsdóttir³

5
6 ¹Geophysical Institute, University of Bergen and Bjerknes Centre for Climate Research, 5007,
7 Bergen, NORWAY.

8 ²Bermuda Institute of Ocean Sciences, St. George's GE01, BERMUDA.

9 ³Institute of Earth Sciences, University of Iceland, Reykjavik, ICELAND.

10
11 Corresponding author: Daniele Zannoni (daniele.zannoni@uib.no)

12
13 **Key Points:**

- 14 • Observation-based non-equilibrium fractionation factors for water isotopologues
15 during ocean evaporation are proposed.
16 • Significant correlation observed between non-equilibrium fractionation factors and 10-m
17 wind speed.
18 • No evidence of distinction is found between smooth and rough regimes for isotopic
19 fractionation during ocean evaporation.

20

21 Abstract

22 Ocean isotopic evaporation models, such as the Craig-Gordon model, rely on the description of
23 non-equilibrium fractionation factors that are, in general, poorly constrained. To date, only a few
24 gradient-diffusion type measurements have been performed in ocean settings to test the validity
25 of the commonly used parametrization of non-equilibrium isotopic fractionation during ocean
26 evaporation. In this work we present six months of water vapor isotopic observations collected
27 from a meteorological tower located in the northwest Atlantic Ocean (Bermuda) with the
28 objective of estimating non-equilibrium fractionation factors (k , ‰) for ocean evaporation and
29 their wind speed dependency. The Keeling plot method and Craig-Gordon model combination
30 was sensitive enough to resolve non-equilibrium fractionation factors during evaporation
31 resulting into mean values of $k_{18} = 5.2 \pm 0.6$ ‰ and $k_2 = 4.3 \pm 3.4$ ‰. Furthermore, we evaluate the
32 relationship between k and 10-m wind speed over the ocean. Such a relationship is expected from
33 current evaporation theory and from laboratory experiments made in the 1970s, but observational
34 evidence is lacking. We show that (i) in the observed wind speed range $[0 - 10 \text{ m s}^{-1}]$ the
35 sensitivity of k to wind speed is small, in the order of -0.2 ‰ m^{-1}s for k_{18} , and (ii) there is no
36 empirical evidence for the presence of a discontinuity between smooth and rough wind speed
37 regime during isotopic fractionation, as proposed in earlier studies. The water vapor d-excess
38 variability predicted under the closure assumption using the k values estimated in this study is in
39 agreement with observations over the Atlantic Ocean.

40

41 Plain Language Summary

42 Phase changes between liquid and vapor continuously occur in the atmospheric water cycle.
43 These phase changes affect the isotopic composition of water through an effect called isotopic
44 fractionation. Depending on the thermodynamic conditions, two types of isotopic fractionation
45 exist: equilibrium and non-equilibrium fractionation. While equilibrium fractionation is
46 relatively well constrained by theoretical considerations from statistical mechanics and
47 laboratory tests, non-equilibrium fractionation is less well constrained theoretically and needs to
48 be investigated by empirical methods. Ocean evaporation is a non-equilibrium process and still
49 today there is little agreement on which are the best non-equilibrium fractionation factors to use
50 in evaporation models. Currently, non-equilibrium fractionation factors are calculated following
51 a parametrization based on wind speed from wind tunnel experiments performed in the 1970s.
52 The reported wind effect has never been directly observed over the ocean. In this study we report
53 non-equilibrium fractionation factors for ocean evaporation estimated directly by measuring
54 water vapor isotopic composition at two heights in an oceanic condition and explore their
55 relationship with wind speed. Since having accurate fractionation factors is fundamental when
56 using stable isotopes to model the Earth's water cycle, the results of this study can help
57 improving the performance of numerical models when describing ocean evaporation.

58 1 Introduction

59 Stable isotopes of hydrogen and oxygen in water have been used successfully for more
60 than 50 years to study processes of the Earth's water cycle. Specifically, using water stable
61 isotopes allows atmospheric processes of the water cycle to be studied on time scales spanning
62 the scale of turbulent eddies to glacial-interglacial time scales (Galewsky et al., 2016).
63 Modulation of the water vapor isotopic composition, hereafter in delta notation, is linked to
64 several physical processes occurring in the atmosphere involving phase change and turbulent
65 mixing. On the one hand, isotope ratios of $^{18}\text{O}/^{16}\text{O}$ ($\delta^{18}\text{O}$) and D/H (δD) in precipitation are

66 largely controlled by upstream precipitation during moisture transport and isotopic equilibrium
67 effect during phase changes (Craig, 1961; Dansgaard, 1964; Rozanski et al., 1993). So-called
68 temperature and continental effects visible on isotopic composition of precipitation are also
69 visible on tropospheric water vapor (Galewsky et al., 2016). On the other hand, the deviation
70 from the linear relationship between $\delta^{18}\text{O}$ and δD (i.e., $\text{d-excess}=\delta\text{D}-8*\delta^{18}\text{O}$) in precipitation is
71 controlled by non-equilibrium effects linked to evaporative conditions of moisture source areas
72 (Craig & Gordon, 1965; Merlivat & Jouzel, 1979), by moisture recycling above the continents
73 (Risi et al., 2013), as well as by sub-cloud droplet evaporation (Stewart, 1975) and cloud
74 microphysics (Ciais & Jouzel, 1994). The d-excess signal in surface water vapor at daily and
75 sub-daily time scale has been shown to be largely affected by local surface fluxes, advection and
76 exchange with the free atmosphere both over land (e.g. Aemisegger et al., 2014) and over the
77 ocean (e.g. Benetti et al., 2014).

78 **1.1 Magnitude and control of non-equilibrium fractionation during ocean evaporation:** 79 **objectives of the study**

80 Isotopic fractionation can occur under two different conditions during water phase
81 change in the hydrological cycle: equilibrium and non-equilibrium. While isotopic fractionation
82 effects under equilibrium conditions above 0°C are well understood, non-equilibrium
83 fractionation effects are still poorly constrained. During evaporation, a non-equilibrium process,
84 the relative weight of molecular and turbulent diffusion controls the magnitude of non-
85 equilibrium fractionation. The molecular diffusivity ratios for $\text{HD}^{16}\text{O}/\text{H}_2^{16}\text{O}$ and $\text{H}_2^{18}\text{O}/\text{H}_2^{16}\text{O}$ in
86 air are 0.9757 and 0.9727 (Merlivat, 1978). However, these need to be scaled in evaporation
87 models because evaporation in an oceanic environment is not a pure molecular diffusion-
88 controlled process but also include a turbulence component, that is not fractionating (Brutsaert,
89 1965, 1975, Craig & Gordon, 1965). To account for this turbulent component, a parametrization
90 of non-equilibrium fractionation factors dependent on wind speed as the only independent
91 variable has been proposed (Merlivat & Coantic, 1975). This parametrization, together with
92 relative humidity (RH) and sea surface temperature (SST), was further used in Merlivat and
93 Jouzel (1979) to model the variability of water vapor d-excess under a global closure assumption
94 (i.e. of a closed water budget). However, several recent studies have questioned the assumed role
95 of SST and wind speed on the controls of non-equilibrium fractionation based on water vapor d-
96 excess observations (Bonne et al., 2019; Steen-Larsen et al., 2014; Pfahl and Wernli, 2008; Pfahl
97 and Sodemann, 2014; Steen-Larsen et al., 2015; Uemura et al., 2008). Other studies argued that
98 water vapor d-excess above the ocean surface may not be influenced solely by ocean surface
99 evaporative conditions, namely RH and SST, but also by the coupling between the Marine
100 Boundary Layer (MBL) and the free troposphere (Benetti et al., 2018; Galewsky et al., 2022) as
101 well as by air-sea interactions during cold and warm advection (Thurnherr et al., 2021).
102 Consequently, it can be concluded that a substantial uncertainty exists on the magnitude of non-
103 equilibrium fractionation during evaporation in real-environmental conditions and, still, no
104 agreement exists on the controls of non-equilibrium fractionation by SST and wind speed (e.g.
105 Gonfiantini et al., 2020). This lack of consensus drives the following questions: which non-
106 equilibrium fractionation factors are the most accurate to use during the evaporation process in
107 the MBL? Is there empirical evidence for a dependency between non-equilibrium effects and
108 wind speed in the oceanic environment? If a relationship between wind speed and non-
109 equilibrium fractionation exists, is it captured by the established parametrizations by Merlivat

110 and Jouzel (1979) which are based on wind tunnel experiments? These research questions will be
111 addressed in this study by:

- 112 1. Estimating the non-equilibrium fractionation factors for $\delta^{18}\text{O}$ and δD that best-fit the
113 observed isotopic composition of the evaporation flux from the ocean surface.
- 114 2. Test the validity of theoretical parametrization of the wind speed effect on non-
115 equilibrium fractionation with observations of the isotopic composition of the
116 evaporation flux over the ocean.

117 The impacts and limitations of the method applied for estimating the non-equilibrium
118 fractionation factors and the isotopic composition of evaporation flux from the ocean surface will
119 be discussed in detail, focusing on potential SST and ocean isotopic composition
120 inhomogeneities in the study area. Furthermore, we will discuss the sensitivity of the linear
121 relationship between d-excess and RH normalized to SST (h_s) under the closure assumption
122 (hereafter, CA) by using the non-equilibrium fractionation factors estimated in this study and
123 other available datasets of water vapor observations in the MBL.

124

125 **1.2 Estimating the isotopic composition of the evaporation flux using near-surface water** 126 **vapor observations**

127 The isotopic composition of the evaporation flux can be estimated by three
128 micrometeorological methods: Eddy Covariance (Braden-Behrens et al. 2019, Wahl et al. 2021),
129 Flux Gradient (FG, Yakir and Wang 1996) and Keeling Plot (KP, Keeling, 1958). The Eddy
130 Covariance method requires high-frequency measurements of wind speed and vapor isotopic
131 composition that are difficult to obtain but provides direct observations of the isotopic
132 composition of the evaporation flux. FG and KP methods do not require high-frequency
133 measurements but rely on assumptions of the environmental conditions during evaporation. In
134 principle, FG and KP can be used to estimate the isotopic composition of the evaporation flux by
135 direct application of a fully turbulent mixing model between two end members: a constant water
136 vapor flux and a background moisture of constant isotopic composition (binary mixing model).
137 In this context, the application of KP and FG methods would be best addressed in an oceanic
138 environment, where the main source of evaporating water is the ocean surface. Keeping the
139 closure assumption valid from a local point of view, i.e. assuming that all the water vapor in the
140 MBL originates from the evaporation flux, single level near-surface observations of the water
141 vapor d-excess should be representative of local evaporative conditions, namely SST, RH and
142 wind speed. This assumption, however, is no longer valid when measurements are performed in
143 low evaporation areas or for periods when other prevailing water vapor exchange processes, such
144 as advection and/or entrainment, occur in the atmosphere. The expected wind speed effect could
145 be smoothed out in the vapor d-excess signal by other processes and observations of water vapor
146 isotopic composition at a single height level then might not be representative of the evaporation
147 flux. Furthermore, variability of the water vapor isotopic composition in the free atmosphere,
148 during advection and via contribution of sea-spray evaporation can introduce errors in the
149 estimation of the isotopic composition of the flux. Therefore, observations at different height
150 levels should be used to estimate the isotopic composition of the evaporation flux with KP and
151 FG instead of single height time series of water vapor isotopic composition. Many profile
152 measurements are available in continental settings from atmospheric research and flux towers
153 (e.g. Griffis et al., 2016) but are scarce over the ocean. Most of the available profile observations

154 over the ocean were acquired over short time frames with cryotrapping (Gat et al., 2003; Craig &
155 Gordon, 1965). More recently, two-heights profiles were obtained during research cruises but
156 some additional uncertainties were introduced due to the use of different instruments for isotopic
157 analysis at each height, ship movement, ship exhaust, and ocean spray contribution to the vapor
158 composition (Thurnherr et al., 2020). In this study we analyze a unique six months (20th June to
159 30th December 2013) data set of continuous observations of water vapor isotopic composition
160 sampled at two heights from a meteorological tower located in the northwest Atlantic region
161 (Bermuda, Figure 1) and use it to estimate the isotopic composition of the ocean evaporation
162 flux.

163 [FIGURE 1]

164 Given that Bermuda is located in part of the source region for the precipitation which is
165 deposited in Greenland, this study is also relevant for ice core science (Johnsen et al., 1989; H.
166 Sodemann et al., 2008), questioning the type of information deduced from d-excess in
167 paleoclimate archives on the evaporative conditions at the source regions such as the role of
168 wind speed and SST (e.g. Jouzel et al., 2007; Steen-Larsen et al., 2011, Markle et al., 2018
169 Osman et al., 2021).

170 **2 Materials and Methods**

171 **2.1 Study site**

172 The study site is located in the south-western part of Bermuda, at the Tudor Hill Marine
173 Atmospheric Observatory (THMAO) operated by Bermuda Institute of Ocean Sciences (32.26°
174 N 64.88° W). The THMAO tower faces the coast (distance ~30m) and is 20.5 m high.
175 Considering the altitude of the tower base (~29 m AMSL), the top of the tower faces the ocean at
176 a height of ~50 m AMSL. The climatic conditions at Bermuda are characterized by a humid
177 subtropical climate, strongly affected by the Gulf Stream. The study area is situated in the so-
178 called Bermuda-Azores High, a large subtropical center of high atmospheric pressure. The high-
179 pressure system is primarily centered near the Bermuda Islands during summer and fall, and near
180 Azores during winter and early spring. Ocean evaporation around Bermuda Island is strong due
181 to its location near the Gulf Stream area and due to cold air advection, especially during the
182 winter (Aemisegger & Papritz 2018). ERA5 reanalysis data (Hersbach et al., 2020) shows that
183 the evaporation flux (E) in the study area exceeds the precipitation flux (P), as expected ($P-E = -$
184 1.34 mm day^{-1}). Analysis with a Lagrangian moisture source diagnostic (Läderach and
185 Sodemann, 2016) for the Jun-Dec 2013 observation period calculated with ERA-Interim
186 reanalysis data (Dee et al., 2011) at a $1^\circ \times 1^\circ$ resolution and a 6h time step revealed that 45% of
187 lower tropospheric moisture originated in a $10^\circ \times 10^\circ$ area around the study site (inset map in
188 Figure 1). The evaporation flux footprint was also evaluated with a flux footprint model (Kljun et
189 al., 2015), suggesting that 90% of the fetch area at the top of THMAO is within 2800 m. Due to
190 its position and climatic conditions, the island of Bermuda is therefore an ideal study site for
191 evaporation-related processes and their control on the d-excess signal because ocean evaporation
192 is the dominant source of the MBL vapor and there is low influence of continental water vapor.

193 **2.2 Meteorological and ocean observations**

194 Air temperature, relative humidity (T, RH, Campbell Scientific EE181-L125-PT), wind speed
195 and wind direction (WS, WD, R.M. Young CAT NO. 05103) were measured at the top inlet (50
196 m AMSL) of THMAO. The wind speed measured at 50 m AMSL was corrected to 10 m AMSL

197 assuming a log-law wind profile and a roughness length of 0.2 mm (Stull, 1997). Sea Level
198 Pressure (SLP) and precipitation (P) were measured ~20 km northeast at the L. F. Wade
199 International Airport (TXKF) by the Bermuda Weather Service. MBL height data was retrieved
200 from ERA5 global reanalysis data (blh variable), which is based on a critical value of the bulk
201 Richardson number and depends on the vertical wind shear and buoyancy (ECMWF, 2017).
202 Gridded blh was retrieved at $0.25^\circ \times 0.25^\circ$ and 1-hour temporal resolution and was linearly
203 interpolated to the study site location.

204 **2.3 SST and Ocean water isotopic composition**

205 Salinity and SST observations are available from buoys inside the reef at 3h time resolution (Hog
206 Reef and Crescent Reef), at St. George Harbor at daily resolution, and outside the reef at
207 monthly resolution for the Bermuda Atlantic Time-series Study (BIOS, 2021). Salinity and SST
208 measurement locations are reported in Figure 1. To minimize potential bias due to local SST
209 variations we chose the averaged Operational Sea Surface Temperature and Sea Ice Analysis
210 (OSTIA, UK MET OFFICE, 2005) data as representative for SST of the study site. High
211 correlation is observed between average SST measured inside the reef and OSTIA product
212 averaged on a $1^\circ \times 1^\circ$ box centered on Bermuda (R Pearson > 0.96) but better agreement, in terms
213 of maximum absolute difference, was observed between BATS and OSTIA data (1.08 °C) than
214 for Crescent reef and OSTIA data (2.55 °C).

215 No measurements of ocean water isotopic composition near the study site are available for the
216 period of interest, but the temporal variability of the ocean isotopic composition in the study area
217 is assumed to be very low. Several sources have been evaluated for estimating the most
218 representative composition of ocean water around the study site: gridded dataset (LeGrande &
219 Schmidt, 2006), North Atlantic cruises published data (Benetti et al., 2014, 2017a) as well as
220 from samples collected at the BATS site two years before this campaign (BIOS, 2021). The
221 isotopic composition of the ocean in this study is assumed to be $\delta^{18}\text{O}_L = 1.09\text{‰}$ and $\delta\text{D}_L =$
222 7.25‰ , which is the average between the isotopic composition calculated with the salinity to
223 isotope conversion (Benetti et al., 2017a) applied to local salinity data (BIOS, 2021) and the
224 ocean isotopic composition estimated from gridded dataset (LeGrande & Schmidt, 2006). Full
225 details on ocean water isotopic composition are reported in Supporting Info, Text S1.

226 **2.4 Water vapor isotopic composition and humidity observations**

227 Ambient air was sampled at THMAO tower at two different heights: 2.5 m and 50 m AMSL.
228 Ambient air was continuously pumped from the two inlets to a manifold located at the tower
229 base that was connected to a Picarro L2120-i isotopic water vapor Cavity Ring-Down
230 Spectroscopy (CRDS) analyzer. Quick air transport was ensured through heated copper tubing
231 using a 10 L min^{-1} sampling pump. The sampling line was switched between the two inlets every
232 15 minutes and when one inlet was connected to the analyzer, the other inlet was flushed by a
233 secondary 5 l min^{-1} pump. This configuration ensured a continuous circulation of air inside the
234 tubing system, thus minimizing the lag and memory effect for the two inlets. The CRDS analyzer
235 sampled water vapor from the main line at its nominal flow rate ($\sim 40 \text{ sccm min}^{-1}$) and recorded
236 humidity and water isotopic composition at $\sim 0.56 \text{ Hz}$ frequency. To reduce the memory effect
237 due to the switching between top and bottom inlet, the first 10 minutes of data after valve
238 switching was removed and the last 5 minutes was averaged. In this way, the 5 minutes average
239 is assumed to be representative of the isotopic composition during measurement for each level,
240 which yields one measurement point per half hour per level. The inlet can be approximated to a

241 first-order low pass filter with transfer function $H=1/(\tau+1)$, where τ is the time the system's
242 response need to reach 63% of the final value for a step change from zero initial condition
243 ($\tau(\delta^{18}\text{O}) = 212$ s, $\tau(\delta\text{D}) = 310$ s). Assuming the final value of the signal to be 1 for a normalized
244 step change, we estimated that the magnitude (mag) of signal attenuation is only -1.9 dB for $\delta^{18}\text{O}$
245 and -3.4 dB for δD ($\text{dB} = 20\log_{10}(\text{mag})$) and the phase difference between $\delta^{18}\text{O}$ and δD signal is
246 $<9^\circ$ with an averaging window of 0.5 hours. The error introduced by signal attenuation and phase
247 difference between $\delta^{18}\text{O}$ and δD signal in the system is considered insignificant at the time
248 resolution used in this study. However, a small persistent bias in d-excess can still be present
249 during monotonically variations of $\delta^{18}\text{O}$ and δD signals.

250 The isotope readings of the water vapor analyzer were calibrated on the VSMOW-SLAP scale
251 (IAEA, 2009) using several laboratory standards at the beginning and towards the end of the
252 observation period. Drift-correction measurements were carried out on a sub-daily basis (every
253 6-12 hours) and humidity-isotope response curves were performed every 1-2 months during the
254 study period to correct for the humidity dependency of water vapor isotopic composition.
255 Precision of water vapor isotopic measurement are expected to be 0.14‰ for $\delta^{18}\text{O}$ and 1.1‰ for
256 δD . The reader is referred to a previous study conducted at THMAO for additional details on the
257 setup of the sensing system, on the calibration protocol and on sensing system performances
258 (Steen-Larsen et al., 2014). Humidity observations of the CRDS analyzer (moist mixing ratio, w
259 [ppmv]) were calibrated against RH observations at the top inlet.

260 **2.5 Estimation of the evaporation flux isotopic composition**

261 The isotopic water vapor observations acquired with the CRDS analyzer represent the time-
262 averaged atmospheric moisture composition at a certain height above sea level. We used the KP
263 method between the two inlets to estimate the isotopic composition of the water vapor flux (δ_E).
264 In the KP method, δ_E is assumed to be equal to the intercept of the linear best-fit model between
265 the isotopic composition of water vapor ($\delta^{18}\text{O}$ or δD) and the inverse of humidity ($1/w$) at the
266 two different height levels. The uncertainties for δ_E (σ_{δ_E}) were calculated as a function of
267 instrument precision, sample size, and atmospheric conditions (Good et al., 2012). However, in
268 our case the number of observations for each time-step is equal to the degrees of freedom
269 required to calculate the uncertainty associated with the flux composition. Therefore,
270 observations were grouped on a daily basis and the error on flux composition was calculated
271 when more than two observations were available. It is important to note that the computation of
272 the flux composition with the KP method is valid only under the following assumptions:

- 273 1. The mixing process in the gradient measurement space is fully turbulent and does not
274 introduce any fractionation: turbulent diffusion is the same for all isotopologues.
- 275 2. Water vapor flux is constant with height: the mixing ratio and water vapor isotopic
276 composition vertical profiles is characterized by a monotonic trend.
- 277 3. Variability of water vapor isotopic signal is not significantly affected by advection or
278 entrainment from the free troposphere during the acquisition of water vapor profiles.
- 279 4. Isotopic composition of source water is constant in the time interval considered.

280 Therefore, water vapor observations were filtered to fulfill the above mentioned assumptions, as
281 further discussed in Section 3.2 and Section 5.1. It is worth noting that the regression method
282 used to calculate the isotopic composition of the evaporation flux can also impact the result, as
283 recently shown in Hu et al. (2021). In this study we used the ordinary least squares method to
284 evaluate the KP intercept. According to Hu et al. (2021), the ordinary least squares method is

285 more robust than e.g. the Geometric Mean Regression method and should be comparable with
 286 the York Solution method under large fetch conditions. In this context, the isotopic composition
 287 of water vapor measured at the top inlet is assumed to be representative of water vapor in the
 288 MBL with a fetch area similar to the one estimated with the moisture diagnostic. However,
 289 because the large height difference between the bottom and top inlets results into different fetch
 290 areas, the water vapor isotopic composition at the bottom inlet was corrected ($\delta^{18}\text{O}=+0.07\text{‰}$ and
 291 $\delta\text{D}=+0.75\text{‰}$) accounting for the SST difference between open ocean SST and reef area SST, as
 292 further discussed in Section 5.2.

293 **2.6 Estimation of non-equilibrium fractionation factors**

294 The Craig-Gordon (CG) (Craig & Gordon, 1965) model was used to calculate δ_E (‰) from the
 295 ocean surface following the notation introduced in Merlivat and Jouzel (1979), as reported in
 296 equation (1):

$$297 \quad \delta_E = (1 - k) \frac{\alpha_{V/L}^{(1+\delta_L)-h_s(1+\delta_A)}}{(1-h_s)} - 1 \quad (1)$$

298 where $\alpha_{V/L}$ [<1] is the equilibrium fractionation factor between vapor and liquid (Horita &
 299 Wesolowski, 1994), h_s [1] is the RH measured at the top of the turbulently mixed sublayer
 300 relative to ocean surface temperature (OSTIA SST [K], averaged on a $1^\circ \times 1^\circ$ box centered on
 301 Bermuda), k [1] is the non-equilibrium fractionation factor, δ_A is the isotopic composition of
 302 atmospheric moisture [1], δ_L is the isotopic composition of the ocean water [1]. The non-
 303 equilibrium fractionation factor k (reported in ‰ hereafter) is estimated from a direct comparison
 304 between the observed (KP) and modeled (CG) isotopic composition of the evaporation flux. For
 305 a given flux observation i , it is possible to calculate m different values of the flux composition
 306 with the CG model by varying the non-equilibrium fractionation factors within a certain range.
 307 The best k values are then calculated by error minimization between the modeled and observed
 308 evaporation flux composition for each pair of top and bottom inlet observations in the filtered
 309 dataset. To estimate the average values of k , the inverse of the errors of the observed flux
 310 composition were used as the weights in the computation of the average. Populations of mean
 311 non-equilibrium fractionation factors k were estimated with bootstrapping, repeating the above
 312 sequence for 10^4 times with random resampling. Additional details on how the non-equilibrium
 313 fractionation factors are calculated are reported in Supporting Info, Text S2 and Text S3.

314 **3 Data description**

315 **3.1 Dataset**

316 Time series of water vapor at the top and bottom inlets were resampled using a common UTC
 317 time indexing with a resolution of 30 minutes through linear interpolation. Meteorological
 318 observations were also averaged and synchronized accordingly to CRDS observations. The water
 319 vapor time series used in this study includes 8793 datapoints, representative of 30-minutes
 320 averaged observations of water vapor isotopic composition at two height levels over the ocean
 321 surface. The complete dataset accounts for 95% coverage of the study period (Figure 2).

322 [Figure 2]

323 Based on d-excess, the pattern of atmospheric water vapor composition can be divided into two
324 main groups: a first group from summer to mid-autumn with gentle daily to weekly d-excess
325 oscillations and a second group, from mid-autumn to early winter, with larger and more
326 pronounced d-excess oscillations at weekly scale. The transition in the d-excess pattern follows
327 the general decrease in humidity and the large h_s variability observed from late October (marked
328 by gray triangles in Figure 2). The temperatures decrease in autumn-winter is also linked to a
329 small shift of the center of mass of moisture sources toward the north-west (not shown). This
330 shift can be linked to the increase in baroclinicity towards autumn and winter and to the more
331 frequent passage of extratropical cyclones over the gulf stream leading to strong ocean
332 evaporation (Aemisegger & Sjolte, 2018).

333 **3.2 Filtered dataset for flux estimation**

334 To guarantee high data quality and for maximizing the validity of assumptions under KP
335 (Section 2.5, points 1 - 4), several constraints were introduced to filter the dataset. The rationale
336 behind those constraints is summarized for each variable in Table 1. By means of the quality
337 control filtering criteria, the sample size is reduced from 8793 to 814 30-minutes averaged
338 observations (~10% of available data). The variables that are most responsible for the exclusion
339 of data points are the daytime and the western wind sector constraints. Just those two filtering
340 criteria account for approximately 85% of rejections. However, these strict filtering criteria were
341 necessary because of the local evapotranspiration signal contribution, with wind blowing from
342 inland and dew formation caused by night cooling. The remaining filtering criteria accounted for
343 an additional 5% of rejections.

344 Most of the observations (~90%) of the filtered dataset were selected between 20th June and 23rd
345 October, as shown in Figure 2. From the perspective of data representativeness, the main features
346 of the dataset after the filtering procedure are: (i) slightly changed mean and median values (for
347 $\delta^{18}\text{O}$ and d-excess) and reduction of secondary modes in d-excess distribution; (ii) statistically
348 significant change in regression parameters for d-excess vs h_s ; (iii) significant reduction of
349 observations characterized by deeper MBL (blh > 1000 m, from 17% to 4%); (iv) change of the
350 wind speed distribution in terms of the mean (from 2.8 ms^{-1} to 4.0 ms^{-1}). Therefore, the main
351 consequences of data reduction are a larger impact of shallow atmospheric mixing, a smaller
352 influence of large MBL development and less periods characterized by low wind speed
353 conditions. More details on the impact of data filtering on the distribution shape of variables of
354 interest are reported in Supporting Info, Text S4.

355 **4 Results**

356 **4.1 The isotopic composition of the evaporation flux (δ_E) from the ocean surface**

357 Descriptive statistics of the evaporation flux isotopic composition from the ocean surface and the
358 water vapor isotopic composition observed at the top inlet during daytime are reported in Table
359 2. On average, the number of data points available for KP calculation is 20 per day and the
360 coefficients of determination for both $\delta^{18}\text{O}$ and δD regression lines are high ($R^2 = 0.78$, on
361 average). For comparison, the Flux Gradient method (FG, Lee et al., 2007) was also used to
362 compute the isotopic composition of evaporation flux, obtaining nearly identical results but
363 different uncertainties, especially for δD ($\sigma_{\delta E} = 0.59\text{‰}$ and 51‰ for $\delta^{18}\text{O}$ and δD , respectively).

364 The high similarity between the FG and KP methods is consistent with other studies (Good et al.,
 365 2012; Hu et al., 2021) which is why we focused on the KP method. As expected, the isotopic
 366 composition of the flux is enriched with respect to the atmospheric water vapor composition and
 367 depleted compared to the ocean isotopic composition. The mean δD of the evaporation flux is
 368 between recent estimates of the global mean HDO fluxes (-37.6‰ following Good et al., 2015)
 369 and estimates made in past studies (-22‰ following e.g. Gat, 1996). No evident trend was
 370 observed for daily δ_E during the study period, for both $\delta^{18}\text{O}$ and δD (Supporting Info, Figure S6).

371 **4.2 Non-equilibrium fractionation factor distributions estimated with flux observations**

372 Non-equilibrium fractionation factors are expressed hereafter in term of k_{18} (for $\delta^{18}\text{O}$) and k_2 (for
 373 δD) to allow a direct comparison with the parametrization proposed in Merlivat and Jouzel
 374 (1979). Applying the bootstrapping method (10^4 samples with 80 observations in each) to the
 375 filtered dataset yields a mean \pm 1 std. dev. $k_{18} = 5.21 \pm 0.64\text{‰}$ and $k_2 = 4.32 \pm 3.41\text{‰}$, as show in
 376 Figure 3.

377 [Figure 3]

378 The obtained k PDFs are in the range predicted by the parametrization proposed in Merlivat and
 379 Jouzel (1979). For k_{18} , the distribution of the mean values falls in the middle of the
 380 parametrizations for the smooth and rough wind speed regimes as proposed by Merlivat and
 381 Jouzel. A similar result was obtained for the average k_2 , the PDF of which is however
 382 characterized by a significantly larger spread. Consistent with previous works, non-equilibrium
 383 fractionation factors are on average $\sim 0.20 - 0.25$ times the value expected for a purely
 384 diffusivity-driven evaporation process (Merlivat, 1978). For reference, the k values estimated in
 385 other studies are also reported in Figure 3 (Pfafl & Wernli, 2009; Uemura et al., 2010). Note that
 386 the k_{18} values estimated in this study are 2-3 ‰ smaller than previous studies and more consistent
 387 with the parametrization of k_{18} proposed in Merlivat and Jouzel (1979). On average the ratio
 388 k_2/k_{18} is equal to 0.83, similar to 0.88 in Merlivat and Jouzel (1979) and 0.84 reported in Luz et
 389 al. (2009).

391 **4.3 Observed relationship between non-equilibrium fractionation factors and 10-m wind speed**

393 To test a dependency of the fractionation factors k on wind speed, the filtered dataset was binned
 394 in 10-m wind speed classes with bin size 0.5 m s^{-1} . For each wind speed class, the non-
 395 equilibrium fractionation factors were calculated using the KP method at 30 min time step.
 396 Afterwards, mean and standard error of k were calculated for each wind speed bin center. Mean
 397 k_{18} values obtained in such way are reported as a function of 10-m wind speed in Figure 4.a.

398 [Figure 4]

399 In the wind speed range $[0.5 - 10] \text{ m s}^{-1}$ the negative correlation between k_{18} and wind speed is
 400 high and statistically significant ($r=-0.72$, $p\text{-value}=1 \times 10^{-3}$). The parametrization proposed in
 401 Merlivat and Jouzel (1979) agrees well with the observed k_{18} variability between 0.5 and 6 m s^{-1} ,
 402 with an average absolute difference of 0.1‰ . Most importantly, the differences between
 403 parametrized and observed k_{18} values are normally distributed around zero (Kolmogorov-
 404 Smirnov and Shapiro-Wilk p-values equals to 0.13 and 0.34, respectively) and the errors can
 405 therefore be attributed to random noise in the measurement. On the other hand, observed k_{18} are
 406 2‰ larger than modeled k_{18} for rough regime parametrization between 6 and 10 m s^{-1} . Moreover,

407 the theoretical wide discontinuity between smooth and rough regime expected at $\sim 6 \text{ m s}^{-1}$ is not
 408 visible in the observations. A decrease of k_{18} in the $7 \pm 1 \text{ m s}^{-1}$ wind speed region is noticeable
 409 but k_{18} observations quickly approach the main decreasing trend. The observed k_{18} values are on
 410 average 1.7‰ higher than the ones calculated with the rough regime parametrization between 7
 411 and 10 m s^{-1} . Despite the small number of observations at wind speed above 7 m s^{-1} , this study:
 412 (i) does not provide sufficient experimental evidence that there are two different regimes in the
 413 wind dependency of k_{18} ; and (ii) suggests that a continuous decrease of k_{18} as a function of wind
 414 speed is more likely in the interval $[0.5 - 10] \text{ m s}^{-1}$. Such a decrease can be approximated by the
 415 following simplified equation:

$$416 \quad k_{18} = (-0.16 \pm 0.04) * \text{WS} + (6.6 \pm 0.3) \% \quad (2)$$

418 where WS is the 10-m wind speed in m s^{-1} . Equation (2) highlights that in the wind speed range
 419 $[0.5 - 10] \text{ m s}^{-1}$ the sensitivity of k_{18} to wind speed is only $-0.16 \pm 0.04 \% \text{ m}^{-1}\text{s}$. Data filtering
 420 prevents to calculate k_{18} at lower wind speed values, mainly because of the thresholds on
 421 humidity and isotopic composition differences between the two inlets. When such thresholds are
 422 removed, the number of observations increases on the left side of the wind speed distribution
 423 (Figure 4.c), with a $\sim 5\%$ increase of the sample size but yields a larger uncertainty for the lowest
 424 wind speed bin (SE=1.7‰, not shown). The impact of the presence/absence of humidity and
 425 isotopic composition difference thresholds between the two inlets is minimal in the k_{18} wind
 426 speed relationship. Indeed, the average absolute difference of k_{18} with/without those thresholds is
 427 only 0.1‰ in the $[0.5 - 10] \text{ m s}^{-1}$ wind speed range, with a minimal increase of the slope of
 428 $0.04\% \text{ m}^{-1}\text{s}$. Unfortunately, the limited number of datapoints above 10 m s^{-1} does not allow any
 429 other speculation on the dependency of k_{18} to higher wind speed and prevents a better
 430 constraining of the rough regime. Furthermore, it is possible that other processes such as sea
 431 spray contribution might start to become important in the net evaporation flux at higher wind
 432 speeds (Andreas et al., 1995; Veron, 2015). Therefore, equation (2) must be considered valid
 433 only in the $[0.5 - 10] \text{ m s}^{-1}$ wind speed range.

434
 435
 436 Continuing with k_2 , observations are scattered and very noisy on the k_2 vs wind speed coordinate
 437 plane (data reported in Supporting Info, Figure S5) because δD is less strongly influenced by
 438 non-equilibrium fractionation than $\delta^{18}\text{O}$. The correlation between k_2 and wind speed is low and
 439 not significant within the $[0.5 - 10] \text{ m s}^{-1}$ wind speed range ($r=-0.34$, $p\text{-value}=0.15$).
 440 Observations are not in agreement with Merlivat and Jouzel (1979) parametrization, neither for
 441 the smooth nor for the rough regime, with an average absolute difference of 1.4‰ from the
 442 model. The noise in k_2 observations drastically affects the variability of the k_2/k_{18} ratio, which
 443 shows an average value of 0.8 and a standard error of 0.1 (Figure 4.b). It is worth noting that the
 444 k_2/k_{18} ratio is not correlated with 10-m wind speed.

445

446 **5. Discussion**

447 **5.1. Method sensitivity to filtering criteria**

448 The KP method is based on assumptions that might partly be violated in a dynamic oceanic
 449 environment. Even on an island in the middle of the ocean, variability of local evaporation
 450 sources due to e.g. vegetation and change in wind direction, can affect the validity of a simplified

451 binary mixing model, with ocean and free atmosphere as the only end members. The strict
 452 filtering criteria used in this study to estimate the isotopic composition of the evaporation flux
 453 and the non-equilibrium fractionation factors tries to select the data for maximizing the validity
 454 of the assumptions behind an ideal binary mixing model. This strict filtering, however, reduced
 455 the original dataset size significantly, as mentioned before. Here we discuss how each filtering
 456 criteria affects the results shown in Section 4.1 - 4.3, removing only data that is affected by
 457 moisture input from precipitation events (Figure 5).

458 [Figure 5]

459 When all the filters are switched off, the isotopic composition of the evaporation flux decreases
 460 significantly and the mean δ_E values are not in accordance what would be expected for
 461 evaporation from the ocean (Gat, 1996; Good et al., 2015; Craig & Gordon, 1965), as shown in
 462 Figure 5.a and b. Both daytime and western wind sector filters enrich the isotopic composition of
 463 the flux. However, westward wind direction has the largest impact on $\delta^{18}\text{O}$ flux while daytime
 464 and westward wind direction filtering contributes likewise on δD flux. This different impact for
 465 $\delta^{18}\text{O}$ and δD fluxes highlights the different sensitivity of the method to environmental changes in
 466 daytime-nighttime temperatures (larger effect on δD , minimal on $\delta^{18}\text{O}$) and on water vapor
 467 sources (ocean source vs local evapotranspiration, similar effect for both δD and $\delta^{18}\text{O}$). The
 468 lower night temperatures, coupled to the poor ventilation due to low wind speeds during the
 469 night, increase RH substantially. Such stable conditions might promote the contribution of
 470 transpiration signal from local vegetation on the moisture near the ground. The k values show the
 471 mirror image of the evaporation flux composition. Indeed, wind direction filtering contributes the
 472 most on decreasing k_{18} value while time and wind direction contribute nearly equally to
 473 decreasing k_2 . Enabling/removing the thresholds on isotopic and humidity differences between
 474 the two inlets have only a marginal impact on the average flux composition and k estimation.

475 **5.2 Impact of ocean surface composition and SST inhomogeneity in the fetch area on k** 476 **estimation**

477 The top and bottom inlets are sensitive to different fetch areas because of the height difference
 478 between the two inlets at THMAO (~48 m). The flux footprint prediction model (Kljun et al.,
 479 2015) suggested that 90% of the fetch area for the bottom inlet is within 100 m while for the top
 480 inlet is within 2800 m. The island of Bermuda is characterized by shallow waters close to the
 481 coast. Therefore, it is possible that local circulation of ocean water within the coral reef system
 482 can have an impact on SST variability and on surface water isotopic composition. Continuous
 483 measurement of SST and ocean isotopic composition covering the whole study area are not
 484 available. However, a first approximation of the variability of SST and salinity (as a proxy of
 485 evaporation) in the study area can be retrieved from buoys and BATS data, as shown in Figure
 486 6.a and Figure 6.c. In this context, the variability of SST can be used to estimate the equilibrium
 487 water vapor variability in the study area (Figure 6.b) while the variability of salinity can be used
 488 to estimate the variability of ocean composition by applying the salinity to isotope conversion
 489 following Benetti et al (2017a) (Figure 6.d).

490 [Figure 6]

491 It is reasonable to assume that OSTIA SST is more representative of the isotopic composition of
 492 equilibrium water vapor for the top inlet while the SST measured near the island coastline is

493 representative for the bottom inlet. To account for the different fetch areas, we correct the water
 494 vapor isotopic composition at the bottom inlet by adding the mean deviation of St. George
 495 equilibrium SST from OSTIA, that is +0.07‰ and +0.75‰ for $\delta^{18}\text{O}$ and δD , respectively (i.e.
 496 the mean of blue PDF in Figure 6.b). As anticipated in Section 2.5, we used this correction to
 497 calculate the isotopic composition of evaporation fluxes shown in this study. Similarly, the ocean
 498 composition within the reef is likely more representative of evaporating water within the reef,
 499 hence, an approximate offset can be added to the isotopic composition of the ocean equal to -
 500 0.06‰ and -0.38‰ for $\delta^{18}\text{O}$ and δD , respectively (i.e. the mean of the green PDF in Figure 6.d).
 501 Next, we discuss how large is the impact of such corrections on the estimation of the k values
 502 and on the relationship between k and wind speed. As shown in Table 3, the inhomogeneity of
 503 ocean composition can introduce a bias in k_{18} and k_2 in the order of 0.3‰ and 1.3‰, respectively.
 504 These biases, are smaller than the uncertainties of k_{18} and k_2 . On the other hand, SST
 505 inhomogeneity in the study area can introduce a 0.8‰ and 8‰ bias in k_{18} and k_2 estimation.
 506 When the SST correction is implemented, the k_{18} bias is still comparable to k_{18} uncertainty while
 507 k_2 differs significantly when the offset is introduced (66% absolute deviation). Therefore, SST
 508 has a larger impact on δD than on $\delta^{18}\text{O}$ and the impact of ocean composition inhomogeneity in
 509 the study area is lower than the impact of SST in the estimation of k_{18} and k_2 . It should be noted
 510 that neither the correction for SST nor the correction for ocean composition take into account the
 511 magnitude of the evaporation flux in the estimation of the average δ_E . The average δ_E should be
 512 in principle weighted by mass flux from the ocean surface. However, similar non-equilibrium
 513 fractionation factors were obtained with an SST correction based on the day-by-day difference
 514 between OSTIA and St. George SST instead of the mean difference during the whole study
 515 period (5.37 and 5.16 for k_{18} and k_2 , respectively). A key point is that SST correction and Salinity
 516 + SST corrections lower the k_2/k_{18} ratio below unity (0.83 and 0.57), which makes sense from the
 517 physical point of view, since the $(1-\text{HD}^{16}\text{O}/\text{H}_2^{16}\text{O})$ quantity needs to be smaller than $(1-$
 518 $\text{H}_2^{18}\text{O}/\text{H}_2^{16}\text{O})$ (e.g. as recently shown in Hellmann & Harvey, 2020). However, when both
 519 salinity and SST corrections are implemented, k_2 is too low and not consistent, e.g. with recent
 520 water vapor observations in the Atlantic Ocean (Bonne et al., 2019). Finally, both corrections do
 521 not significantly affect the observed correlation between k_{18} and wind speed. The main effect of
 522 the corrections on k_{18} and k_2 leads to shifts in the distributions without changing their shapes.
 523 This means that the effect introduced by the correction is translated into changing the intercept of
 524 the best fit line of Figure 4.a but keeping the slope mostly unchanged. The observed negative
 525 correlation between k_{18} and wind speed is robust, regardless of the correction implemented.

526 **5.3 Suggested k values and limitations of the approach**

527 The large footprint difference for the two inlets is the highest source of uncertainty and the
 528 limitation in our experimental setup, even with the strict filtering criteria applied to the dataset.
 529 The good agreement of our results with previous studies of the evaporation flux isotopic
 530 composition and the expected k_2/k_{18} ratio in the expected range cannot serve as validation of our
 531 method, but they provide a constraint on identifying the highest uncertainty source. As outlined
 532 in section 5.2, we identified SST differences in the footprint areas to be the main driver for the
 533 systematic bias observed for k_2 . Given that SST correction does not affect k_{18} significantly, we
 534 suggest using the mean value of $k_{18}=5.2\%$ and $k_2=4.3\%$. Indeed, these k values are estimated
 535 using all the observations that maximized the validity of KP method assumptions and thus should
 536 be representative for the average conditions. When simulating ocean evaporation in isotope-

537 enabled General Circulation Models, k_{18} can be calculated from the 10-m wind speed using the
 538 empirical linear relationship (equation 2) and k_2 can be estimated by the average observed ratio
 539 of $k_2/k_{18}=0.83$. These values are valid for wind speed between 0.5 and 10 m s⁻¹.

540 **5.4 D-excess sensitivity to evaporative conditions using suggested k values**

541 Assuming that the water vapor d-excess signal is only modulated by local evaporation, the
 542 suggested non-equilibrium fractionation factors of this study can be used to predict water vapor
 543 d-excess [‰] using h_s [‰] and the CA. Table 4 reports the regression coefficients (slope and
 544 intercept) of the observed and modeled d-excess vs h_s relationship using the data of this study
 545 and the data of four research cruises (Benetti et al., 2017b) which crossed the Atlantic Ocean
 546 between 2012 and 2015 at different latitudes (plots of d-excess vs h_s reported in Figure S3 and
 547 Figure S7 of Supporting Information). For computation of d-excess under CA, ocean $\delta^{18}\text{O}$ was
 548 obtained from the LeGrande and Schmidt (2006) gridded dataset, by averaging the closest 4 grid
 549 points of the ship location for each cruise, and ocean δD was estimated from the $\delta^{18}\text{O}$ vs δD
 550 relationships (Benetti et al. 2017a). The slope of the modeled d-excess vs h_s relationship is fully
 551 comparable with the one calculated for STRASSE cruise only. In general, the MAE and RMSE
 552 increase as a function of the latitude for cruises, with negligible errors for PIRATA and
 553 STRASSE. When screening the Bermuda dataset as shown in Section 3.2, the CA yields smaller
 554 regression coefficients in absolute values (-0.46 ‰/‰ and 46 ‰ for slope and intercept,
 555 respectively). A further decrease can be observed when the dataset is screened also by removing
 556 observations with MBL height e.g. larger than 1000 m (-0.39 ‰/‰ and 40‰). Given that
 557 regression coefficients for Bermuda tend to agree with the one predicted under the CA and that
 558 the STRASSE cruise was characterized by shallow boundary layer (Benetti et al., 2014),
 559 atmospheric mixing between the MBL and the free atmosphere can be one of the processes
 560 causing the discrepancy between observed d-excess variability in the MBL and the CA. Indeed,
 561 such a process (i) promotes the variability of the isotopic composition of water vapor in the free
 562 atmosphere and (ii) modulates h_s in the MBL at the same time (Benetti et al., 2018; Risi et al.,
 563 2019). Although an input of water vapor from the free atmosphere violates assumption #3 in the
 564 KP method to calculate δ_E (see section 2.5), we do not observe a significant change in estimation
 565 of δ_E and k values when screening also for MBL height ($\delta^{18}\text{O}_E = -3.08\text{‰}$ and $\delta\text{D}_E = -23.06\text{‰}$;
 566 $k_{18} = 5.16\text{‰}$ and $k_2 = 4.08\text{‰}$). A regression model based on observed d-excess, CA and MBL
 567 height is able to reproduce 82% of the d-excess signal variability in the entire Bermuda dataset,
 568 showing that the 55% of variability can be attributed to h_s variability and 22% to MBL height
 569 variability. Although this simplified analysis considers h_s and the height of the MBL as two
 570 independent quantities, even though they are correlated, it shows that d-excess signal in MBL
 571 water vapor might contain more information than evaporative conditions over the ocean surface.
 572 We therefore expect this study to highlight the need for more research effort to determine the
 573 processes driving d-excess signal in the MBL at the daily – subdaily scale.

574 **6 Conclusions**

575 Profile observations of water vapor isotopic composition near the ocean surface can be used to
 576 quantify the impact of non-equilibrium effects on isotopic fractionation during oceanic
 577 evaporation. In this study we provided a unique dataset of water vapor isotope observations
 578 collected at two different heights on a meteorological tower in Bermuda, located in the North
 579 Atlantic Ocean. Using the combination of the Keeling Plot method and the Craig-Gordon model

580 we have calculated the non-equilibrium fractionation factors for $^{18}\text{O}/^{16}\text{O}$ and D/H during ocean
581 evaporation and investigated their dependency on wind speed. A strict data filtering approach
582 was used to maximize the validity of the assumptions behind the Keeling Plot method, ensuring a
583 robust estimate of the non-equilibrium fractionation factors. The observed non-equilibrium
584 fractionation factor for $^{18}\text{O}/^{16}\text{O}$ is in good agreement with the established smooth wind speed
585 parametrization in Merlivat and Jouzel (1979) (mean \pm 1 std. dev $k_{18}=5.2 \pm 0.6\%$). We find a
586 statistically significant correlation between k_{18} and 10-m wind speed, with a sensitivity in the
587 order of -0.16 to $-0.20 \text{‰ m}^{-1} \text{ s}$. Such low sensitivity would be nearly impossible to resolve by
588 conventional measurements of the isotopic composition of water vapor at a single height above
589 the ocean surface. Although the number of observations in high wind speed conditions is sparse
590 in the observational dataset, the observed relationship between k_{18} and wind speed does not
591 provide a clear indication for the presence of a discontinuity between a smooth and rough surface
592 under different wind regimes. In fact, the rough regime parametrization of k_{18} underestimates the
593 observed fractionation factor by a factor of ~ 0.66 . Mean non-equilibrium fractionation factor for
594 D/H were shown to be in the range expected following Merlivat and Jouzel (1979) albeit with a
595 larger uncertainty (mean \pm 1 std. dev $k_2=4.3 \pm 3.4\%$). We showed that the spatial inhomogeneity
596 of SST and ocean isotopic composition around the study site have an impact on the estimation of
597 k_2 and its uncertainty because of the large height difference between the two inlets and the
598 resulting different fetch areas. The results for k_{18} are robust regardless of different data filtering
599 and are insensitive to footprint correction based on the spatial variability of SST and ocean
600 composition. Lastly, using the non-equilibrium fractionation factors of this study and the closure
601 assumption we showed that the d-excess signal in water vapor at the daily – subdaily temporal
602 scale over the ocean contains information on Marine Boundary Layer height in addition to SST
603 and RH. The results of this study allow more accurate simulation of d-excess in the MBL, hence
604 allowing observations to be used to improve the fidelity of isotope enabled numerical models
605 when simulating ocean evaporation.

606 **Acknowledgments**

607 The work was supported by the Danish Council for Independent Research – Natural Sciences
608 grant number 10-092850 and the Carlsberg Foundation, and the AXA Research Fund. The Tudor
609 Hill Marine Atmospheric Observatory in Bermuda was supported by NSF award OCE1829686.
610 We acknowledge an infrastructure grant (nr. 10/0244) from the Icelandic Research Council
611 (Rannis), that partly covered the cost of the Picarro facilities in Bermuda. HCSL and DZ
612 acknowledges funding from the European Union’s Horizon 2020 research and innovation
613 programme under grant agreement no. 821868. H.S. acknowledges support by the Norwegian
614 Research Council (Project SNOWPACE, grant no. 262710) and by the European Research
615 Council (Consolidator Grant ISLAS, project no. 773245). SW acknowledges funding from the
616 European Research Council (ERC) under the European Union’s Horizon 2020 research and
617 innovation program: Starting Grant-SNOWISO (grant agreement 759526).

618

619 **Open Research**

620 The water vapor time series used for calculating the non-equilibrium fractionation factors in the
621 study is available on Pangea, DOI to be minted with CC BY 4.0 (Steen-Larsen et al.,
622 2022). Code for data analysis and for reproducing plots in the article is available here:
623 <https://doi.org/10.5281/zenodo.6977090>.

624

625 **References**

- 626 Aemisegger, F., Pfahl, S., Sodemann, H., Lehner, I., Seneviratne, S. I., & Wernli, H. (2014).
 627 Deuterium excess as a proxy for continental moisture recycling and plant transpiration.
 628 *Atmospheric Chemistry and Physics*, 14(8), 4029–4054. [https://doi.org/10.5194/acp-14-](https://doi.org/10.5194/acp-14-4029-2014)
 629 [4029-2014](https://doi.org/10.5194/acp-14-4029-2014)
- 630 Aemisegger, F., & Sjolte, J. (2018). A climatology of strong large-scale ocean evaporation
 631 events. Part II: Relevance for the deuterium excess signature of the evaporation flux.
 632 *Journal of Climate*, 31(18), 7313–7336. <https://doi.org/10.1175/JCLI-D-17-0592.1>
- 633 Andreas, E. L., Edson, J. B., Monahan, E. C., Rouault, M. P., & Smith, S. D. (1995). The spray
 634 contribution to net evaporation from the sea: A review of recent progress. *Boundary-Layer*
 635 *Meteorology*, 72(1–2), 3–52. <https://doi.org/10.1007/BF00712389>
- 636 Benetti, M., Reverdin, G., Pierre, C., Merlivat, L., Risi, C., Steen-larsen, H. C., & Vimeux, F.
 637 (2014). Deuterium excess in marine water vapor: Dependency on relative humidity and
 638 surface wind speed during evaporation. *Journal of Geophysical Research: Atmospheres*,
 639 119, 584–593. <https://doi.org/10.1002/2013JD020535>
- 640 Benetti, M., Reverdin, G., Aloisi, G., & Sveinbjörnsdóttir, Á. (2017a). Stable isotopes in surface
 641 waters of the Atlantic Ocean: Indicators of ocean-atmosphere water fluxes and oceanic
 642 mixing processes. *Journal of Geophysical Research: Oceans*, 122(6), 4723–4742.
 643 <https://doi.org/10.1002/2017JC012712>
- 644 Benetti, M., Steen-Larsen, H. C., Reverdin, G., Sveinbjörnsdóttir, Á. E., Aloisi, G.,
 645 Berkelhammer, M. B., et al. (2017b). Data Descriptor: Stable isotopes in the atmospheric
 646 marine boundary layer water vapour over the Atlantic Ocean, 2012-2015. *Scientific Data*,
 647 4, 1–17. <https://doi.org/10.1038/sdata.2016.128>
- 648 Benetti, M., Lacour, J. L., Sveinbjörnsdóttir, A. E., Aloisi, G., Reverdin, G., Risi, C., et al.
 649 (2018). A Framework to Study Mixing Processes in the Marine Boundary Layer Using
 650 Water Vapor Isotope Measurements. *Geophysical Research Letters*, 45(5), 2524–2532.
 651 <https://doi.org/10.1002/2018GL077167>
- 652 BIOS. (2021). Bermuda Atlantic Time-series Study (BATS). <http://bats.bios.edu/> (Last accessed
 653 on: 14/05/2021).
- 654 Bonne, J. L., Behrens, M., Meyer, H., Kipfstuhl, S., Rabe, B., Schöncke, L., et al. (2019).
 655 Resolving the controls of water vapour isotopes in the Atlantic sector. *Nature*
 656 *Communications*, 10(1), 1–10. <https://doi.org/10.1038/s41467-019-09242-6>
- 657 Braden-Behrens, J., Markwitz, C., & Knohl, A. (2019). Eddy covariance measurements of the
 658 dual-isotope composition of evapotranspiration. *Agricultural and Forest Meteorology*,
 659 269–270(January), 203–219. <https://doi.org/10.1016/j.agrformet.2019.01.035>
- 660 Brutsaert, W. (1965). A model for evaporation as a molecular diffusion process into a turbulent
 661 atmosphere. *Journal of Geophysical Research*, 70(20), 5017–5024.
 662 <https://doi.org/10.1029/jz070i020p05017>
- 663 Brutsaert, W. (1975). A theory for local evaporation (or heat transfer) from rough and smooth
 664 surfaces at ground level. *Water Resources Research*, 11(4), 543–550.
 665 <https://doi.org/10.1029/WR011i004p00543>
- 666 Ciais, P., & Jouzel, J. (1994). Deuterium and oxygen 18 in precipitation: isotopic model,
 667 including mixed cloud processes. *Journal of Geophysical Research*, 99(D8).
 668 <https://doi.org/10.1029/94jd00412>

- 669 Craig, H. (1961). Isotopic variations in meteoric waters. *Science*, 133(3465), 1702–1703.
670 <https://doi.org/10.1126/science.133.3465.1702>
- 671 Craig, H., & Gordon, L. I. (1965). *Stable Isotopes in Oceanographic Studies and*
672 *paleotemperatures*. Lischi e Figli, Pisa 122.
- 673 Dansgaard, W. (1964). Stable isotopes in precipitation. *Tellus*, 16(4), 436–468.
674 <https://doi.org/10.3402/tellusa.v16i4.8993>
- 675 Dee, D. P., Uppala, S. M., Simmons, A. J., Berrisford, P., Poli, P., Kobayashi, S., et al. (2011).
676 The ERA-Interim reanalysis: Configuration and performance of the data assimilation
677 system. *Quarterly Journal of the Royal Meteorological Society*, 137(656), 553–597.
678 <https://doi.org/10.1002/qj.828>
- 679 [ECMWF \(2017\), IFS Documentation CY43R3 - Part IV: Physical processes.](http://dx.doi.org/10.21957/efyk72kl)
680 <http://dx.doi.org/10.21957/efyk72kl>
- 681 Galewsky, J., Steen-Larsen, H. C., Field, R. D., Worden, J., Risi, C., & Schneider, M. (2016).
682 Stable isotopes in atmospheric water vapor and applications to the hydrologic cycle.
683 *Reviews of Geophysics*, 54(4), 809–865. <https://doi.org/10.1002/2015RG000512>
- 684 Galewsky, J., Jensen, M. P., & Delp, J. (2022). Marine Boundary Layer Decoupling and the
685 Stable Isotopic Composition of Water Vapor. *Journal of Geophysical Research:*
686 *Atmospheres*, 127(3), 1–14. <https://doi.org/10.1029/2021jd035470>
- 687 Gat, J. R. (1996). Oxygen and Hydrogen Isotopes in the Hydrologic Cycle. *Annual Review of*
688 *Earth and Planetary Sciences*, 24(1), 225–262.
689 <https://doi.org/10.1146/annurev.earth.24.1.225>
- 690 Gat, J. R., Klein, B., Kushnir, Y., Roether, W., Wernli, H., Yam, R., & Shemesh, A. (2003).
691 Isotope composition of air moisture over the Mediterranean Sea: An index of the air-sea
692 interaction pattern. *Tellus, Series B: Chemical and Physical Meteorology*, 55(5), 953–965.
693 <https://doi.org/10.3402/tellusb.v55i5.16395>
- 694 Geernaert, G. L. (2003). Boundary Layers | Surface Layer. *Encyclopedia of Atmospheric*
695 *Sciences*, (1988), 305–311. <https://doi.org/10.1016/b0-12-227090-8/00092-0>
- 696 Gonfiantini, R., Wassenaar, L. I., & Araguas-Araguas, L. J. (2020). Stable isotope fractionations
697 in the evaporation of water: The wind effect. *Hydrological Processes*, 34(16), 3596–3607.
698 <https://doi.org/10.1002/hyp.13804>
- 699 Good, S. P., Soderberg, K., Wang, L., & Caylor, K. K. (2012). Uncertainties in the assessment of
700 the isotopic composition of surface fluxes: A direct comparison of techniques using laser-
701 based water vapor isotope analyzers. *Journal of Geophysical Research Atmospheres*,
702 117(15), 1–22. <https://doi.org/10.1029/2011JD017168>
- 703 Good, S. P., Noone, D., Kurita, N., Benetti, M., & Bowen, G. J. (2015). D/H isotope ratios in the
704 global hydrologic cycle. *Geophysical Research Letters*, 42(12), 5042–5050.
705 <https://doi.org/10.1002/2015GL064117>
- 706 Griffis, T. J., Wood, J. D., Baker, J. M., Lee, X., Xiao, K., Chen, Z., et al. (2016). Investigating
707 the source, transport, and isotope composition of water vapor in the planetary boundary
708 layer. *Atmospheric Chemistry and Physics*, 16(8), 5139–5157. <https://doi.org/10.5194/acp-16-5139-2016>
- 709
- 710 Hellmann, R., & Harvey, A. H. (2020). First-Principles Diffusivity Ratios for Kinetic Isotope
711 Fractionation of Water in Air. *Geophysical Research Letters*, 47(18).
712 <https://doi.org/10.1029/2020GL089999>
- 713 Hersbach, H., Bell, B., Berrisford, P., Hirahara, S., Horányi, A., Muñoz-Sabater, J., et al. (2020).
714 The ERA5 global reanalysis. *Quarterly Journal of the Royal Meteorological Society*,

- 715 146(730), 1999–2049. <https://doi.org/10.1002/qj.3803>
- 716 Hijmans, R. J. (2015). Boundary, Bermuda, 2015. [https://maps.princeton.edu/catalog/stanford-](https://maps.princeton.edu/catalog/stanford-nw036zp7611)
- 717 [nw036zp7611](https://maps.princeton.edu/catalog/stanford-nw036zp7611) (Last accessed on: 14/05/2021).
- 718 Horita, J., & Wesolowski, D. J. (1994). Liquid-vapor fractionation of oxygen and hydrogen
- 719 isotopes of water from the freezing to the critical temperature. *Geochimica et*
- 720 *Cosmochimica Acta*, 58(16), 3425–3437. [https://doi.org/10.1016/0016-7037\(94\)90096-5](https://doi.org/10.1016/0016-7037(94)90096-5)
- 721 Horita, J., Rozanski, K., & Cohen, S. (2008). Isotope effects in the evaporation of water: A status
- 722 report of the Craig-Gordon model. *Isotopes in Environmental and Health Studies*, 44(1),
- 723 23–49. <https://doi.org/10.1080/10256010801887174>
- 724 Hu, Y., Xiao, W., Wei, Z., Welp, L. R., Wen, X., & Lee, X. (2021). Determining the Isotopic
- 725 Composition of Surface Water Vapor Flux From High-Frequency Observations Using
- 726 Flux-Gradient and Keeling Plot Methods. *Earth and Space Science*, 8(3), 1–15.
- 727 <https://doi.org/10.1029/2020EA001304>
- 728 IAEA. (2009). Reference sheet for international measurement standards - SMOW Vienna
- 729 Standard Mean Ocean.
- 730 Johnsen, S. J., Dansgaard, W., & White, J. W. C. (1989). The origin of Arctic precipitation under
- 731 present and glacial conditions. *Tellus, Series B*, 41 B(4), 452–468.
- 732 <https://doi.org/10.3402/tellusb.v41i4.15100>
- 733 Jouzel, J., Stievenard, M., Johnsen, S. J., Landais, A., Masson-Delmotte, V., Sveinbjornsdottir,
- 734 A., et al. (2007). The GRIP deuterium-excess record. *Quaternary Science Reviews*, 26(1–
- 735 2), 1–17. <https://doi.org/10.1016/j.quascirev.2006.07.015>
- 736 Keeling, C. D. (1958). The concentration and isotopic abundances of atmospheric carbon dioxide
- 737 in rural areas. *Geochimica et Cosmochimica Acta*, 13, 322–324.
- 738 [https://doi.org/10.1016/0016-7037\(58\)90033-4](https://doi.org/10.1016/0016-7037(58)90033-4)
- 739 Kljun, N., Calanca, P., Rotach, M. W., & Schmid, H. P. (2015). A simple two-dimensional
- 740 parameterisation for Flux Footprint Prediction (FFP). *Geoscientific Model Development*,
- 741 8(11), 3695–3713. <https://doi.org/10.5194/gmd-8-3695-2015>
- 742 Lee, X., Kim, K., & Smith, R. (2007). Temporal variations of the 18O/16O signal of the whole-
- 743 canopy transpiration in a temperate forest. *Global Biogeochemical Cycles*, 21(3), 1–12.
- 744 <https://doi.org/10.1029/2006GB002871>
- 745 Läderach, A. and Sodemann, H., 2016: A revised picture of the atmospheric moisture residence
- 746 time, *Geophysical Research Letters*, 43, 924-933. <https://doi.org/10.1002/2015GL067449>
- 747 LeGrande, A. N., & Schmidt, G. A. (2006). Global gridded data set of the oxygen isotopic
- 748 composition in seawater. *Geophysical Research Letters*, 33(12), 1–5.
- 749 <https://doi.org/10.1029/2006GL026011>
- 750 Luz, B., Barkan, E., Yam, R., & Shemesh, A. (2009). Fractionation of oxygen and hydrogen
- 751 isotopes in evaporating water. *Geochimica et Cosmochimica Acta*, 73(22), 6697–6703.
- 752 <https://doi.org/10.1016/j.gca.2009.08.008>
- 753 Madsen, M. V., Steen-Larsen, H. C., Hörhold, M., Box, J., Berben, S. M. P., Capron, E., et al.
- 754 (2019). Evidence of Isotopic Fractionation During Vapor Exchange Between the
- 755 Atmosphere and the Snow Surface in Greenland. *Journal of Geophysical Research:*
- 756 *Atmospheres*, 124(6), 2932–2945. <https://doi.org/10.1029/2018JD029619>
- 757 Markle, B. R., Steig, E. J., Roe, G. H., Winckler, G., & McConnell, J. R. (2018). Concomitant
- 758 variability in high-latitude aerosols, water isotopes and the hydrologic cycle. *Nature*
- 759 *Geoscience*, 11(11), 853–859. <https://doi.org/10.1038/s41561-018-0210-9>
- 760 Merlivat, L., & Coantic, M. (1975). Study of mass transfer at the air-water interface by an

- 761 isotopic method. *Journal of Geophysical Research*, 80(24), 3455–3464.
762 <https://doi.org/10.1029/jc080i024p03455>
- 763 Merlivat, L. (1978). Molecular diffusivities of H₂16O, HD16O, and H₂18O in gases. *The*
764 *Journal of Chemical Physics*, 69(6), 2864–2871. <https://doi.org/10.1063/1.436884>
- 765 Merlivat, L., & Jouzel, J. (1979). Global climatic interpretation of the deuterium-oxygen 18
766 relationship for precipitation. *Journal of Geophysical Research: Oceans*, 84(C8), 5029–
767 5033. <https://doi.org/10.1029/JC084iC08p05029>
- 768 NOAA. (2019). Bermuda 1 arc-second Coastal Digital Elevation Model.
769 [https://www.ncei.noaa.gov/metadata/geoportal/rest/metadata/item/gov.noaa.ngdc.mgg.dem](https://www.ncei.noaa.gov/metadata/geoportal/rest/metadata/item/gov.noaa.ngdc.mgg.dem:5010/html)
770 [:5010/html](https://www.ncei.noaa.gov/metadata/geoportal/rest/metadata/item/gov.noaa.ngdc.mgg.dem:5010/html) (Last accessed on: 14/05/2021).
- 771 Osman, M. B., Smith, B. E., Trusel, L. D., Das, S. B., McConnell, J. R., Chellman, N., et al.
772 (2021). Abrupt Common Era hydroclimate shifts drive west Greenland ice cap change.
773 *Nature Geoscience*, 14(10), 756–761. <https://doi.org/10.1038/s41561-021-00818-w>
- 774 Pfahl, S., & Sodemann, H. (2014). What controls deuterium excess in global precipitation?
775 *Climate of the Past*, 10(2), 771–781. <https://doi.org/10.5194/cp-10-771-2014>
- 776 Pfahl, S., & Wernli, H. (2009). Lagrangian simulations of stable isotopes in water vapor: An
777 evaluation of nonequilibrium fractionation in the Craig-Gordon model. *Journal of*
778 *Geophysical Research Atmospheres*, 114(D20), 1–12.
779 <https://doi.org/10.1029/2009JD012054>
- 780 Pfahl, S., & Wernli, H. (2008). Air parcel trajectory analysis of stable isotopes in water vapor in
781 the eastern Mediterranean. *Journal of Geophysical Research Atmospheres*, 113(D20), 1–
782 16. <https://doi.org/10.1029/2008JD009839>
- 783 Risi, C., Noone, D., Frankenberg, C., & Worden, J. (2013). Role of continental recycling in
784 intraseasonal variations of continental moisture as deduced from model simulations and
785 water vapor isotopic measurements. *Water Resources Research*, 49(7), 4136–4156.
786 <https://doi.org/10.1002/wrcr.20312>
- 787 Risi, C., Galewsky, J., Reverdin, G., & Briant, F. (2019). Controls on the water vapor isotopic
788 composition near the surface of tropical oceans and role of boundary layer mixing
789 processes. *Atmospheric Chemistry and Physics*, 19(19), 12235–12260.
790 <https://doi.org/10.5194/acp-19-12235-2019>
- 791 Rozanski, K., Araguás-Araguás, L., & Gonfiantini, R. (1993). Isotopic Patterns in Modern
792 Global Precipitation. *Geophysical Monograph*, 78, 1–36.
793 <https://doi.org/10.1029/gm078p0001>
- 794 Sodemann, H., Schwierz, C., & Wernli, H. (2008). Interannual variability of Greenland winter
795 precipitation sources: Lagrangian moisture diagnostic and North Atlantic Oscillation
796 influence. *Journal of Geophysical Research Atmospheres*, 113(3), 1–17.
797 <https://doi.org/10.1029/2007JD008503>
- 798 Steen-Larsen, H. C., Masson-Delmotte, V., Sjolte, J., Johnsen, S. J., Vinther, B. M., Bréon, F.
799 M., et al. (2011). Understanding the climatic signal in the water stable isotope records from
800 the NEEM shallow firn/ice cores in northwest Greenland. *Journal of Geophysical*
801 *Research Atmospheres*, 116(6), 1–20. <https://doi.org/10.1029/2010JD014311>
- 802 Steen-Larsen, H. C., Sveinbjörnsdóttir, A. E., Peters, A. J., Masson-Delmotte, V., Guishard, M.
803 P., Hsiao, G., et al. (2014). Climatic controls on water vapor deuterium excess in the
804 marine boundary layer of the North Atlantic based on 500 days of in situ, continuous
805 measurements. *Atmospheric Chemistry and Physics*, 14(15), 7741–7756.
806 <https://doi.org/10.5194/acp-14-7741-2014>

- 807 Steen-Larsen, H. C., Sveinbjörnsdóttir, A. E., Jonsson, T., Ritter, F., Bonne, J. -L., Masson-
808 Delmotte, V., et al. (2015). Moisture sources and synoptic to seasonal variability of North
809 Atlantic water vapor isotopic composition. *Journal of Geophysical Research Atmospheres*,
810 *120*. <https://doi.org/10.1002/2015JD023234>
- 811 Steen-Larsen, H. C., Peters, A. J., Wahl, Sveinbjörnsdóttir, Á. E., Zannoni, D. (2022). Calibrated
812 stable water vapor isotope data at 2.5 m ASL and 50 m ASL from Tudor Hill Marine
813 Atmospheric Observatory, Bermuda. *PANGAEA*, [Dataset]
814 <https://doi.org/10.1594/PANGAEA.949607>
- 815 Stewart, M. K. (1975). Stable isotope fractionation due to evaporation and isotopic exchange of
816 falling waterdrops: Applications to atmospheric processes and evaporation of lakes.
817 *Journal of Geophysical Research*, *80*(9), 1133–1146.
818 <https://doi.org/10.1029/jc080i009p01133>
- 819 Stull, R. B. (1997). *An Introduction to Boundary Layer Meteorology*. Springer.
- 820 Thurnherr, I., Kozachek, A., Graf, P., Weng, Y., Bolshiyakov, D., Landwehr, S., et al. (2020).
821 Meridional and vertical variations of the water vapour isotopic composition in the marine
822 boundary layer over the Atlantic and Southern Ocean. *Atmospheric Chemistry and Physics*,
823 *20*(9), 5811–5835. <https://doi.org/10.5194/acp-20-5811-2020>
- 824 Thurnherr, I., Hartmuth, K., Jansing, L., Gehring, J., Boettcher, M., Gorodetskaya, I., et al.
825 (2021). The role of air–sea fluxes for the water vapour isotope signals in the cold and warm
826 sectors of extratropical cyclones over the Southern Ocean. *Weather and Climate Dynamics*,
827 *2*(2), 331–357. <https://doi.org/10.5194/wcd-2-331-2021>
- 828 Uemura, R., Matsui, Y., Yoshimura, K., Motoyama, H., & Yoshida, N. (2008). Evidence of
829 deuterium excess in water vapor as an indicator of ocean surface conditions. *Journal of*
830 *Geophysical Research Atmospheres*, *113*(19), 1–10. <https://doi.org/10.1029/2008JD010209>
- 831 Uemura, R., Barkan, E., Abe, O., & Luz, B. (2010). Triple isotope composition of oxygen in
832 atmospheric water vapor. *Geophysical Research Letters*, *37*(4), 1–4.
833 <https://doi.org/10.1029/2009GL041960>
- 834 UK MET OFFICE. (2005). OSTIA L4 SST Analysis. Ver. 1.0. PO.DAAC.
835 <https://doi.org/https://doi.org/10.5067/GHOST-4FK01>
- 836 Veron, F. (2015). Ocean spray. *Annual Review of Fluid Mechanics*, *47*, 507–538.
837 <https://doi.org/10.1146/annurev-fluid-010814-014651>
- 838 Wahl, S., Steen-Larsen, H. C., Reuder, J., & Hörhold, M. (2021). Quantifying the Stable Water
839 Isotopologue Exchange Between the Snow Surface and Lower Atmosphere by Direct Flux
840 Measurements. *Journal of Geophysical Research Atmospheres*, *126*(13), 1–24.
841 <https://doi.org/10.1029/2020JD034400>
- 842 Yakir, D., & Wang, X. F. (1996). Fluxes of CO₂ and water between terrestrial vegetation and the
843 atmosphere estimated from isotope measurements. *Nature*, *380*(6574), 515–517.
844 <https://doi.org/10.1038/380515a0>
- 845 Zannoni, D. (2022). Bermuda-NEFF, Release of code to calculate non-equilibrium fractionation
846 factors after first cycle of peer review. [Software] <https://doi.org/10.5281/zenodo.6977090>

847 **Figure 1:** Study site in Bermuda. Bermuda Island shape in white color and ocean depth as color scale (Hijmans,
 848 2015; NOAA, 2019); position of Tudor Hill Marine Atmospheric Observatory (white dot) and wind sector (red
 849 lines) to discriminate local transpired water vapor from ocean water vapor (N180° to N340°). Colored circles and
 850 triangle are the sampling locations of available salinity (S) and SST time series around the study area. The large-
 851 scale map on the left shows the location of Bermuda (cross) in the northwest Atlantic Ocean and the main water
 852 vapor sources during the study period. The highlighted sector includes 45% of accounted water vapor uptakes.

853

854 **Figure 2:** Timeseries of water vapor isotopic composition and relevant meteorological parameters at the study site.
 855 **(a, b)** Water vapor isotopic composition, **(c)** mixing ratio and **(d)** wind speed (WS) measured at top inlet height (50
 856 m AMSL). SST data from OSTIA reported as a blue line. **(e)** h_s is the relative humidity measured at top inlet and
 857 normalized to OSTIA SST. Gray triangles on the top and bottom of the figure represent the autumn transition, as
 858 detected from d-excess variability at weekly scale. Observations selected for estimating the isotopic composition of
 859 the evaporation flux are highlighted in red.

860

861 **Figure 3:** Non-equilibrium fractionation factors estimated from flux observations (KP method). Continuous kernel
 862 density function was estimated with bandwidths 0.1‰ and 0.6‰ for k_{18} **(a)** and k_2 **(b)**, respectively. Shaded area
 863 represents the k intervals predicted for smooth (green, 10-m wind speed range [1-6] m s⁻¹) and rough (cyan, 10-m
 864 wind speed range [6-13] m s⁻¹) regimes following Merlivat and Jouzel (1979). For reference, molecular diffusivity
 865 ratios M78 (Merlivat, 1978) and non-equilibrium fractionation factors for ocean settings PW09 (Pfahl & Wernli,
 866 2009) and U10 (Uemura et al., 2010) are reported as vertical dashed lines.

867

868 **Figure 4:** Observed relationship between k_{18} and 10-m wind speed. **(a)** mean \pm standard error of k_{18} estimated for
 869 each wind speed class. Green and cyan lines show the parametrization of k_{18} for smooth and rough wind regimes,
 870 respectively (Merlivat & Jouzel, 1979). Solid black line represents a linear fit ($R^2=0.52$) in the wind speed interval
 871 0.5 – 10 m s⁻¹ (fit equation reported in text). **(b)** k_2/k_{18} ratio for each wind speed class. Dashed black line is the
 872 average ratio (0.8). **(c)** Number of observations and mean wind direction (arrows) for each bin. In all panels: black
 873 lines, black symbols and black bars for filtered dataset; gray lines, gray symbols and gray bars for filtered dataset
 874 with no isotope and humidity thresholds implemented (Table 1, rows 3 and 4): red line, red symbols and red bars
 875 highlight wind speed classes with number of observations ≤ 2 .

876

877 **Figure 5:** Sensitivity of the method for estimating δ_E and k values to filtering criteria. Following Table 1: only
 878 precipitation filter (All off, $n = 6834$), time + precipitation filter (Time, $n = 2016$), wind sector + precipitation (WD,
 879 $n = 3143$), isotopic gradient + precipitation (iso, $n = 3883$), humidity gradient+ precipitation (w, $n = 6484$). **(a)** and
 880 **(b)** sensitivity of isotopic composition of evaporation flux (δ_E) for $\delta^{18}O$ and δD , respectively. **(c)** and **(d)** sensitivity
 881 of non-equilibrium fractionation factors for k_{18} and k_2 , respectively. For all panels, gray shaded areas represent mean
 882 ± 1 std. deviation when enabling all filtering steps.

883 **Figure 6:** SST and salinity inhomogeneity of ocean waters around the study site. **(a)** Time series of SST in different
 884 points of the study area, see Figure 1 for reference of sampling sites. Vertical lines represent selected observations
 885 for flux estimation. **(b)** PDFs of $\delta^{18}O$ and δD [Equilibrium vapor (SST reef) – Equilibrium vapor (SST OSTIA)],
 886 where SST reef is the SST measured in different points within the reef area. **(c)** Similar to (a) but for salinity. **(d)**
 887 PDFs of $\delta^{18}O$ and δD [Ocean Composition (S reef) – Ocean Composition (S BATS)], where S reef is the salinity
 888 measured at different points within the reef area and S BATS is salinity measured at the BATS site. Conversion of
 889 salinity to isotopic composition following Benetti et al. (2017a).

890

891 **Table 1:** List of variables and constraints adopted to filter the time series.

Variable	Indexing	Range/Value	Rejected (cumulative)	Assumption #	Rationale
Time	Time	Daytime observations based on sunrise-sunset hour (LST) with 2 hours symmetrical offset	71%	2,4	No influence of dew formation caused by night cooling
WD	Wind sector inclusion	Western Sector 180°N – 340°N (i.e. excluding winds from inland)	85%	3,4	No influence of local evapotranspiration from vegetation
δD and $\delta^{18}O$	$ \delta D_{\text{Bottom}} - \delta D_{\text{Top}} $ $ \delta^{18}O_{\text{Bottom}} - \delta^{18}O_{\text{Top}} $	> 1 ‰ > 0.1 ‰	89%	2	Difference between Top/Bottom larger than instrumental precision (L2120-i)
w	$w_{\text{Bottom}} - w_{\text{Top}}$	> 100 ppmv*	89%	2	w decreases with height above ocean
P	Time	No precipitation within the last two hours	90%	1,2,3,4	No vapor recycling from precipitation

892
893 The column “rejected” reports the size of dataset that does not fulfill each filtering threshold. Assumption n# refers
894 to the numbered list in Section 2.5. * This is a conservative estimate of instrumental precision not reported in the
895 L2120-i datasheet.
896

897 **Table 2:** Descriptive statistics of evaporation flux and top inlet water vapor isotopic composition at the daily
 898 timescale. Interquartile range (IQR) estimated by fitting a normal PDF on observed δ_E distribution. $\sigma_{\delta E}$ following
 899 Good et al., (2012).

	Mean (‰)	Median (‰)	IQR (‰)	$\sigma_{\delta E}$ (‰)
Evaporation flux $\delta^{18}\text{O}$	-3.37	-4.48	-6.7 ; -0.04	1.17
Evaporation flux δD	-24.99	-33.48	-48.38 ; -1.60	7.33
Top inlet water vapor $\delta^{18}\text{O}$	-11.30	-10.97	-12.10 ; -10.51	-
Top inlet water vapor δD	-78.13	-76.14	-83.15 ; -73.10	-

900

901 **Table 3:** Impact of SST and Ocean composition variability on k_2 , k_{18} and on k_{18} vs wind speed parameters
 902 estimation. Uncertainties are: 0.6‰, 3.5‰, 0.04 and 0.3 for k_{18} , k_2 , slope and intercept, respectively. Deviations
 903 from k values obtained without applying any correction.

Correction	Cause	k_{18} (‰)	Dev. (%)	k_2 (‰)	Dev. (%)	k_2/k_{18}	Slope (‰ m ⁻¹ s)	Interc. (‰)
No correction	-	6.0	-	12.74	-	2.11	-0.20	7.93
Salinity correction	Different isotopic composition of surface water in fetch area	5.8	-4	11.37	-11	1.96	-0.21	7.72
SST correction	SST inhomogeneity in fetch area	5.2	-14	4.32	-66	0.83	-0.16	6.59
Salinity + SST corrections	SST and surface composition inhomogeneity	5.0	-18	2.81	-78	0.57	-0.17	6.37

904

905 **Table 4:** D-excess [‰] vs h_s [‰] relationship: observed and modeled under CA. Observations from ACTIV, RARA,
 906 STRASSE and PIRATA cruises averaged over 15 min (Benetti et al. 2017b). Slopes and intercepts reported with
 907 their (\pm standard error). For modeled d-excess, standard error of the slope is always <0.01 . Mean Absolute Error
 908 (MAE) and Root Means Squared Error (RMSE) of observed d-excess vs modeled d-excess (CA).

Dataset	SST source	Observed d-excess		Modeled d-excess		MAE (‰)	RMSE (‰)
		Slope (‰/‰)	Interc. (‰)	Slope (‰/‰)	Interc. (‰)		
ACTIV (n = 3087)	OSTIA (200 km x 200 km)	-0.32 (\pm 0.01)	33.71 (\pm 0.46)	-0.40	34.43 (\pm 0.07)	6.52	3.47
RARA (n = 5115)	On board SBE38 (1.50 m depth)	-0.38 (<0.01)	39.58 (\pm 0.20)	-0.43	41.58 (\pm 0.23)	2.60	2.46
STRASSE (n = 2224)	On board SBE35 (3.50 m depth)	-0.38 (\pm 0.01)	38.35 (\pm 0.40)	-0.38	38.51 (\pm 0.12)	1.12	1.44
PIRATA (n = 2662)	On board SBE3S (3.33 m depth)	-0.24 (\pm 0.01)	29.37 (\pm 0.47)	-0.41	40.83 (\pm 0.18)	0.89	0.93
Bermuda this study (n = 8791)	OSTIA (1°x1°)	-0.48 (<0.01)	47.91 (\pm 0.16)	-0.36	35.48 (\pm 0.04)	3.82	4.46

Figure 1.

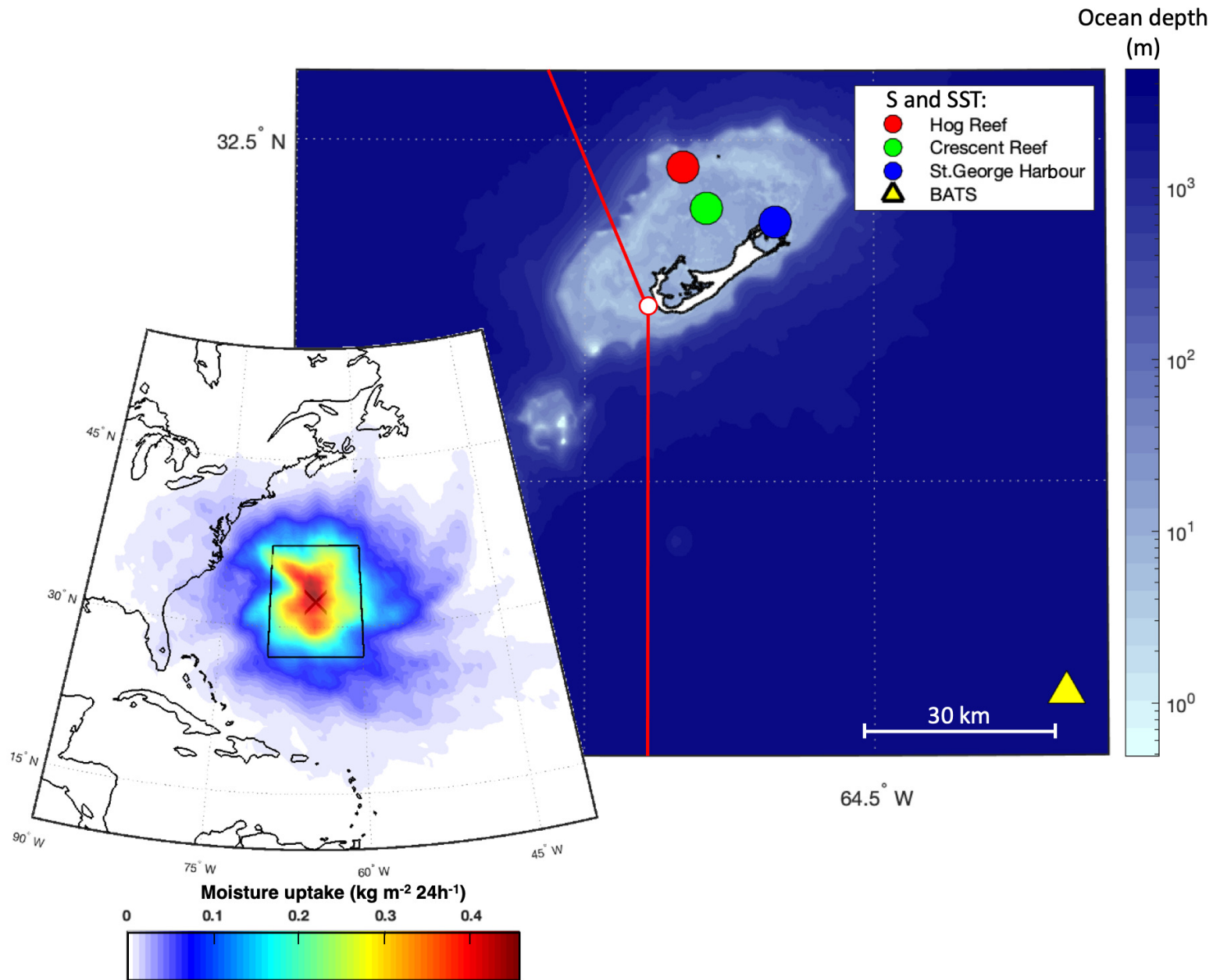


Figure 2.

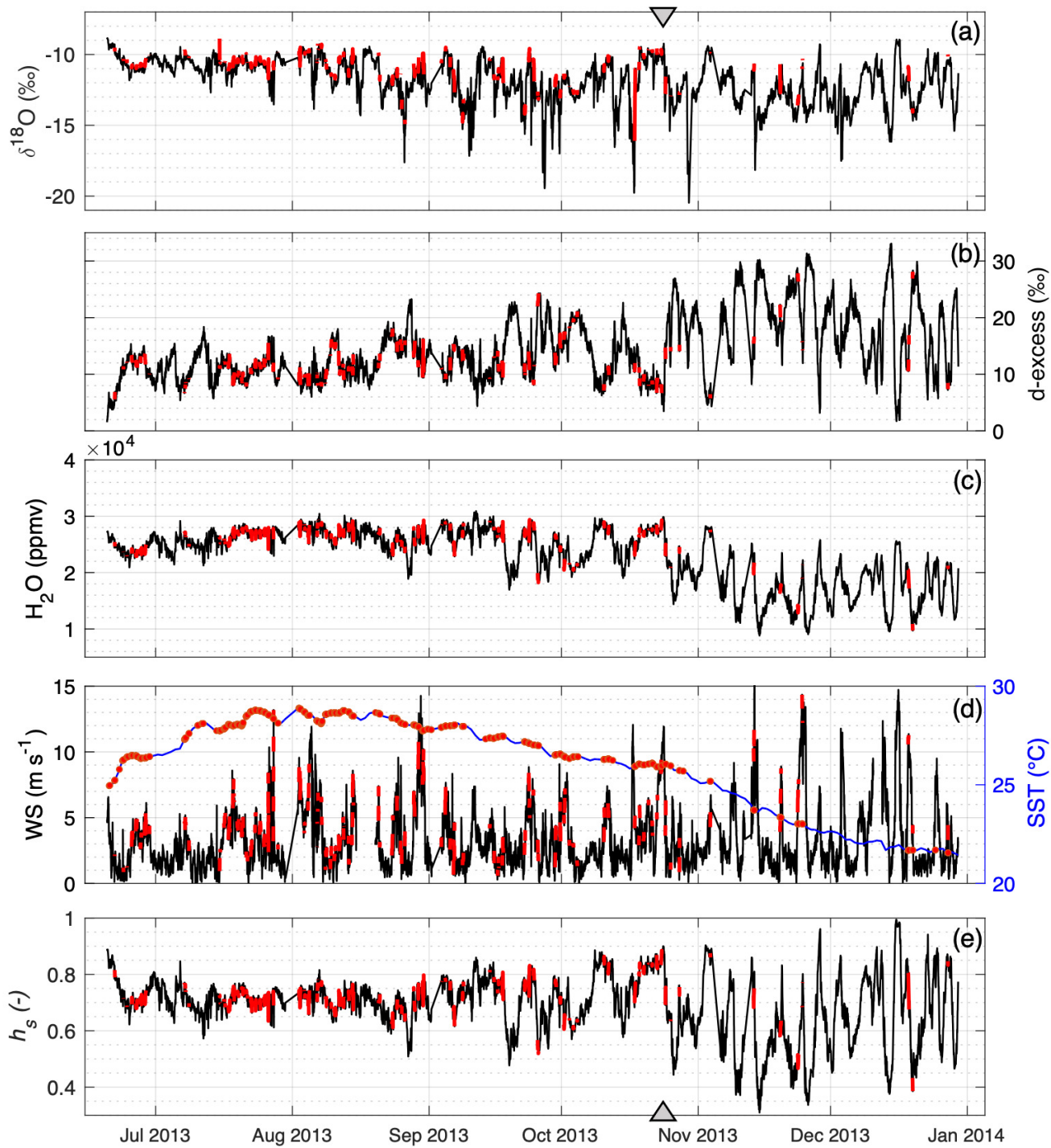


Figure 3.

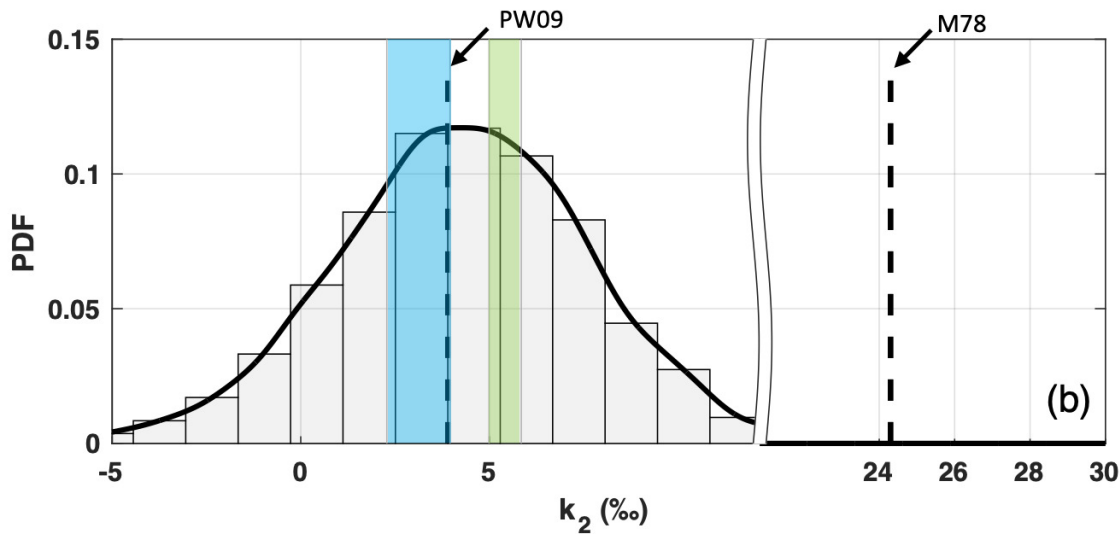
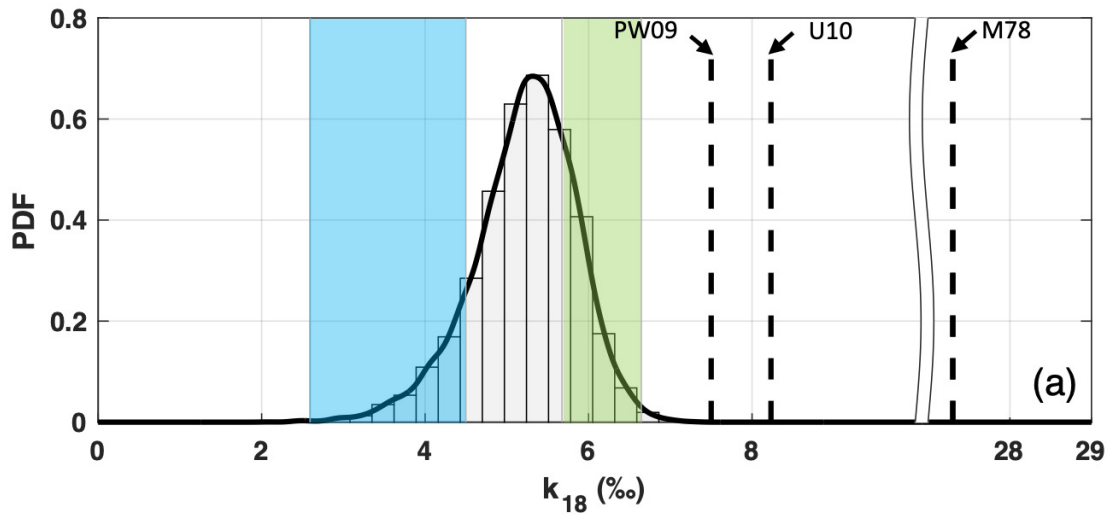


Figure 4.

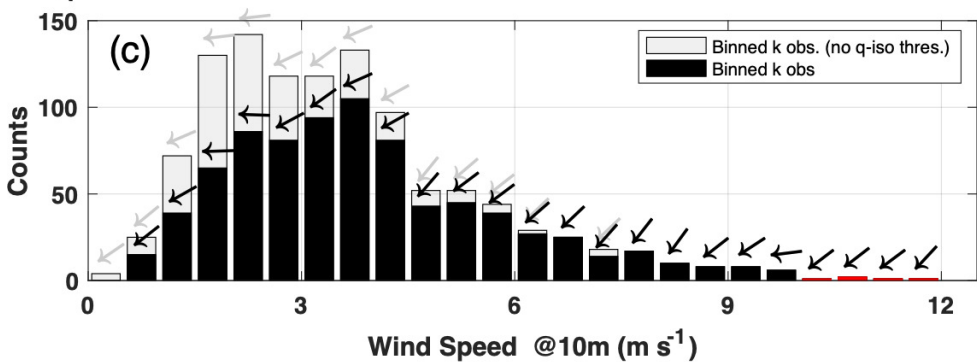
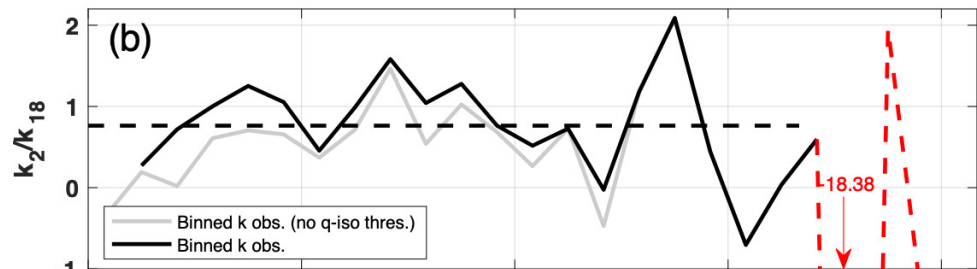
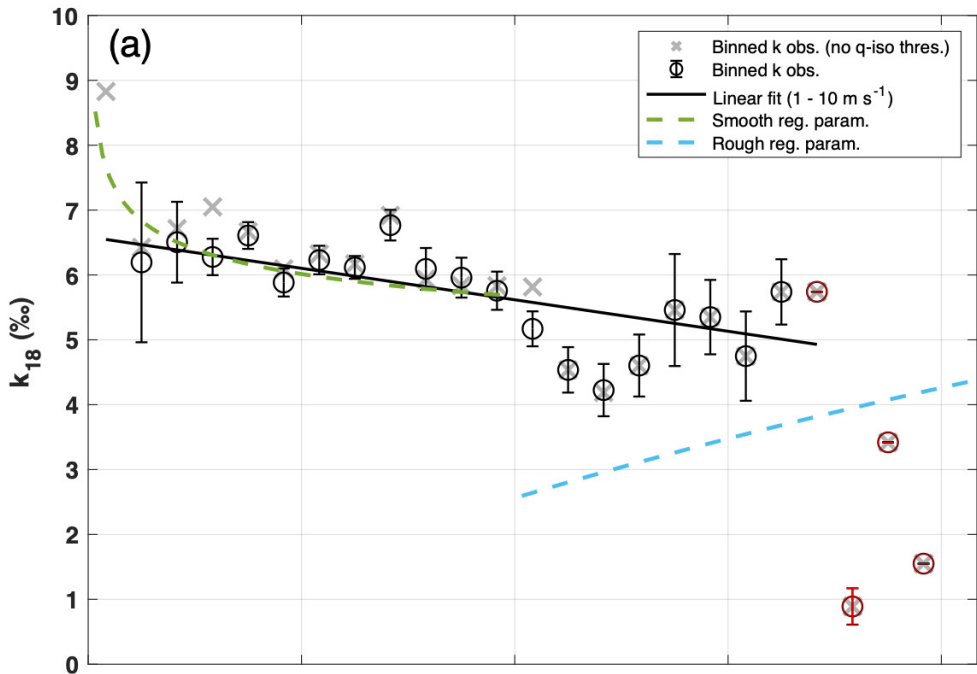


Figure 5.

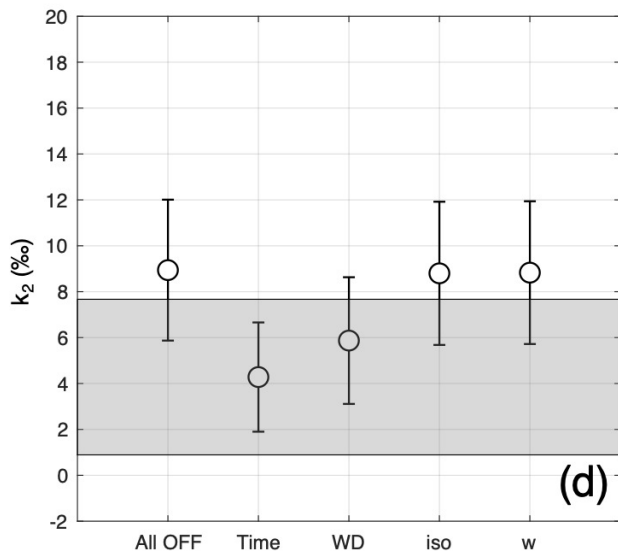
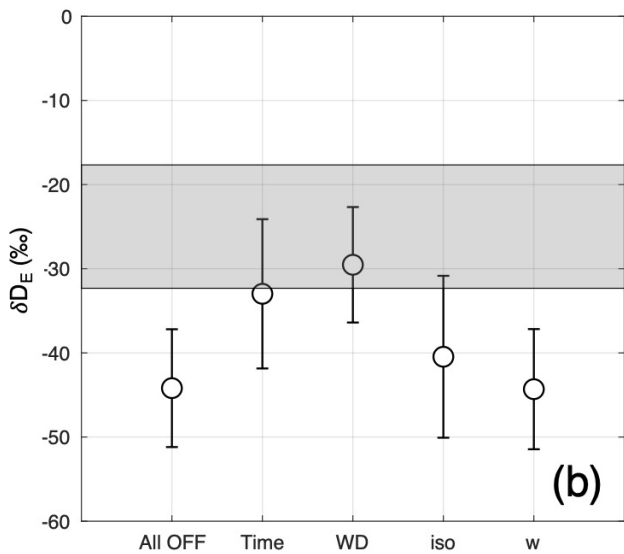
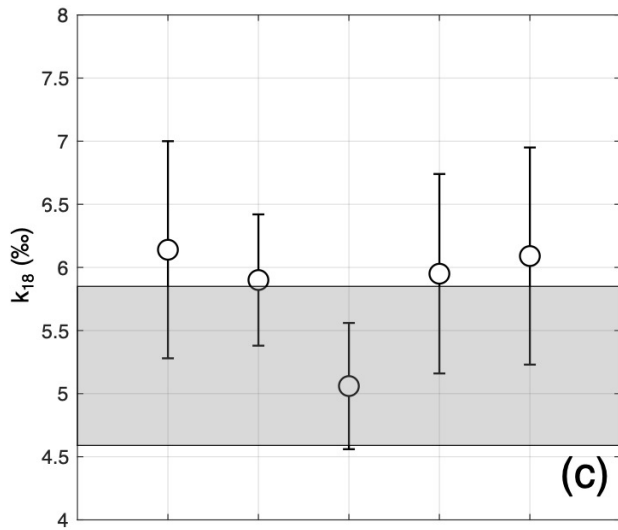
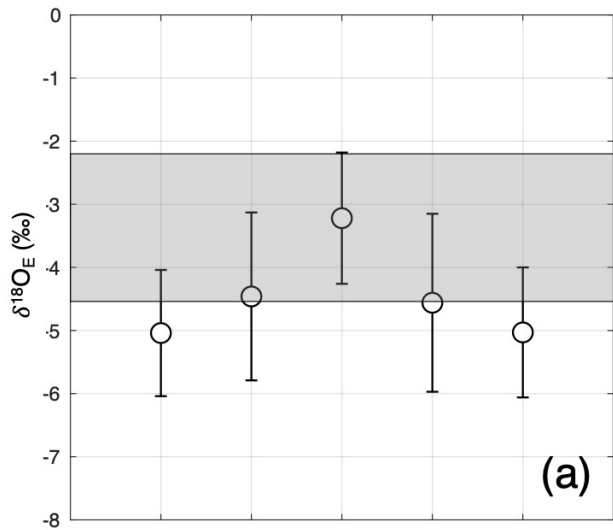


Figure 6.

